ACS Catalysis
Research Article
pubs.acs.org/acscatalysis

Promoting Effects of In_2O_3 on Co_3O_4 for CO Oxidation: Tuning O_2 Activation and CO Adsorption Strength Simultaneously

Yang Lou,† Jian Ma,† Xiaoming Cao, Li Wang, Qiguang Dai, Zhenyang Zhao, Yafeng Cai, Wangcheng Zhan, Yanglong Guo, P. Hu, Guanzhong Lu,* and Yun Guo*

Key Laboratories for Advanced Materials, Research Institute of Industrial Catalysis, East China University of Science and Technology, 130 Meilong Road, Shanghai 200237, China

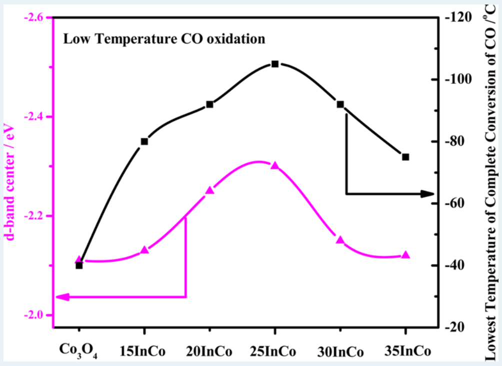

ABSTRACT: The doping of In_2O_3 significantly promoted the catalytic performance of Co_3O_4 for CO oxidation. The activities of $In_2O_3-Co_3O_4$ increased with an increase in In_2O_3 content, in the form of a volcano curve. Twenty-five wt % $In_2O_3-Co_3O_4$ (25 InCo) showed the highest CO oxidation activity, which could completely convert CO to CO_2 at a temperature as low as −105 °C, whereas it was only −40 °C over pure Co_3O_4. The doping of In_2O_3 induced the expansion of the unit cell and structural distortion of Co_3O_4, which was confirmed by the slight elongation of the Co−O bond obtained from EXAFS data. The red shift of the UV−vis absorption illustrated that the electron transfer from O^{2-} to Co^{3+}/Co^{2+} became easier and implied that the bond strength of Co−O was weakened, which promoted the activation of oxygen. Low-temperature H_2-TPR and O_2-TPD results also revealed that $In_2O_3-Co_3O_4$ behaved with excellent redox ability. The XANES, XPS, XPS valence band, and FT-IR data exhibited that the CO adsorption strength became weaker due to the downshift of the d-band center, which correspondingly weakened the adsorption of CO_2 and obviously inhibited the accumulation of surface carbonate species. In short, the doping of In_2O_3 induced the structural defects, modified the surface electronic structure, and promoted the redox ability of Co_3O_4, which tuned the adsorption strength of CO and oxygen activation simultaneously.

KEYWORDS: *Co_3O_4, In_2O_3, CO oxidation, CO adsorption strength, redox ability, surface carbonate species*

1. INTRODUCTION

The development of novel catalysts for low-temperature CO elimination has great value not only in academic research but also in practical application, such as purifying automobile emission and preferential oxidation (PROX) in the proton exchange membrane fuel cell.[1−17] Compared with supported noble metal catalysts,[1−5] transition metal oxides (TMOs), with low cost and high activities, have exhibited a broad range of application and scientific research interest in the field of CO oxidation.

Among the TMOs, Co_3O_4 has been considered as an alternative to a noble metal because of the high activity for low-temperature CO oxidation.[6−14,16,18] In the ideal Co_3O_4 structure,[18] the unit-cell contained eight elemental cells in which one-eighth of the available tetrahedral sites (8a Wyckoff sites) were occupied by Co^{2+} and half of octahedral sites (16d Wyckoff sites) were occupied by Co^{3+}. The advantages of low Co−O bond energy, strong ability of CO adsorption, and high capability to activate oxygen played crucial roles in the CO oxidation over Co_3O_4.[7−19] Haruta et al.[7] reported that Co_3O_4 exhibited excellent low-temperature activity for CO oxidation that T_{50} (the temperature corresponding to the 50% conversion of CO) could be obtained at −54 °C. Xie et al.[10] reported that the primarily exposed [110] plane of Co_3O_4 nanorods could completely catalyze CO oxidation at a temperature as low as −77 °C and could sustain 100% CO conversion to CO_2 during the initial 6 h.

In general, the main four steps in CO oxidation included (1) CO adsorption, (2) the formation of active oxygen, (3) CO reacting with active oxygen, and (4) CO_2 desorption. For CO oxidation on Co_3O_4, some results proposed that the adsorption of CO over Co^{3+} or Co^{2+} sites was the crucial step and that the activated CO could easily react with adjacent lattice oxygen.[10,14,20,21] Meanwhile, the activation of oxygen was also believed to play a very important role in the CO oxidation.[11−14] The catalytic activity of metal oxides for CO oxidation could be obviously promoted by creating much more oxygen vacancies like prereduction with CO pulse[22] or other appropriate pretreatments.[13] In the previous references, many methods had been proposed to promote the catalytic activity of Co_3O_4 either to increase the adsorption sites for CO[10,20,23] or to enhance oxygen activation.[6,11,13,24,25]

However, the effects of CO adsorption strength were usually overlooked, which could influence the coupling of adsorbed CO with activated O and the desorption of CO_2. Too strong adsorption of CO would cause a higher reaction barrier[26] and

Received: July 12, 2014
Revised: October 3, 2014
Published: October 6, 2014

dx.doi.org/10.1021/cs501049r | *ACS Catal.* 2014, 4, 4143−4152

stronger CO_2 adsorption,[27] which could lead to severe accumulation of surface carbonate species. The surface carbonate species were considered as one possible reason for the deactivation of CO oxidation over Co_3O_4,[10−14] which could cause the surface reconstruction[11] and local change of oxidation state.[23] DFT results also confirmed the surface carbonate species could tightly occupy the active sites and inhibit the reaction of CO oxidation on the surface of Co_3O_4.[14]

Therefore, with the assumption of sufficient CO adsorption, simultaneously reducing CO adsorption strength and further enhancing O_2 activation should be an efficient method to promote CO oxidation on Co_3O_4. A general principle of how to choose a suitable doping heteroatom was proposed in our previous paper:[28] lower M−O bonding energies, larger cation radii, and relatively lower electronegativity.

In this work, we selected indium as doping cation to comprehensively present a strategy of tuning CO adsorption strength and O_2 activation simultaneously to promote the catalytic performance of CO oxidation over Co_3O_4.

2. EXPERIMENTAL SECTION

2.1. Preparation of Catalysts. The samples were prepared by precipitation or coprecipitation methods, the cobalt acetate ($Co(CH_3COO)_2{\cdot}4H_2O$) and indium chloride ($InCl_3$) were used as precursor salts, and sodium carbonate (Na_2CO_3) was used as precipitant. The details of preparation were similar to previous work.[6,10,25] Cobalt acetate (4.98 g) and an appropriate amount of $InCl_3$ were dissolved into 80 mL of ethylene glycol, and then the system was degassed by mechanical pump. Then the mixture was heated to 160 °C and kept in N_2 flow for 40 min. Two hundred milliliters of a 0.22 M Na_2CO_3 solution heated at 80 °C was added into the above solution, and the mixture was further aged at 160 °C for 1 h under vigorously stirring. The precipitate was washed using distilled water until no Cl^- was detected by $AgNO_3$ solution. After filtering, the solid powder obtained was dried at 65 °C overnight and calcined at 350 °C for 4 h in air. The calculated contents of In_2O_3 were 15, 20, 25, 30, and 35 wt %, respectively. The prepared catalysts were denoted as *x*InCo where *x* represented the contents of In_2O_3.

2.2. Measurements of Catalytic Activity. The activity of catalysts for CO oxidation was tested in a fixed-bed reactor at atmospheric pressure, and 200 mg catalyst (40−60 mesh) was used. The feed gas containing 1 vol % CO, 20 vol % O_2, and N_2 balance was passed through the catalytic bed at a flow rate of 50 mL/min. The concentrations of CO and CO_2 in the outlet stream were measured by an online gas chromatograph (Fuli 9790 equipped with hydrogen flame ionization detector). Before the experiments, the catalyst was pretreated at 350 °C for 40 min in 20 vol % O_2/N_2 (50 mL/min). The dry feed gas was obtained by passing the feed gas through a cooled trap.

2.3. Structure Characterization. The XRD spectra were obtained with Rigaku D/max 2550 VB/PC diffractometer using a Cu Kα radiation (λ = 1.54056 Å). The X-ray tube was operated at 40 kV and 100 mA. The intensity data was collected at room temperature in a 2θ range from 10° to 70° with a scan rate of 6°/min. The average crystalline size of samples was calculated by the Scherrer formula based on the diffraction peak broadening.

Laser Raman spectra (LRS) of samples were collected at ambient condition on a Renishaw spectrometer. A laser beam (λ= 514 nm) was used for an excitation. The laser beam intensity and the spectrum slit width were 2 mW and 3.5 cm^{-1}, respectively.

The BET surface areas were measured by nitrogen adsorption at liquid nitrogen temperature by using a surface area and porosity analyzer (Quantachrome NOVA 4000e apparatus). Before measurement, the samples were degassed at 180 °C for 6 h in vacuum.

2.4. Temperature-Programmed Reduction and Desorption. The temperature-programmed reduction of H_2 (H_2-TPR) was performed from −80 °C to −50 °C. The catalyst of 50 mg was heated in the flow of 5 vol % H_2/N_2 (20 mL/min) at a heating rate of 10 °C/min. The amount of H_2 consumption during the process of reduction was measured by a thermal conductivity detector (TCD).

The temperature-programmed desorption of O_2 (O_2-TPD) was performed from −80 to 0 °C using the same apparatus. The procedures were as follows: (1) catalysts (200 mg) were cooled to −80 °C with O_2 adsorption for 1 h; (2) purging with He for 1 h; (3) heating at a rate of 10 °C/min from −80 to 0 °C. The signal of O_2 desorption from the samples was measured by a TCD.

Before H_2-TPR and O_2-TPD, the samples were pretreated by 20 vol % O_2/N_2 (50 mL/min) mixed gas at 350 °C for 40 min.

2.5. UV−vis Absorption Spectroscopy. UV−vis absorption spectroscopy measurements for the Co_3O_4 and In_2O_3−Co_3O_4 samples were carried out on a Cary 500 (U.S Varian) spectrometer, equipped with an integration sphere. The spectra were recorded in the wavelength range of 200−800 nm. The samples were dispersed into ethanol solvent and ultrasonicated before the measurement.

2.6. X-ray Photoelectron Spectroscopy (XPS). The XPS was investigated in an AXIS-Ultra-DLD spectrometer (Kratos Analytical) using a monochromated Al Kα X-ray source (1486.6 eV). The XPS spectra of the selected elements were measured with the constant analyzer pass energy of 80.0 eV. All binding energies (BEs) were referred to the adventitious C 1s peak (BE = 284.8 eV). The peaks were fitted according to ref 29.

2.7. XPS Valence Band Spectra. The valence band photoemission spectra were conducted on a Thermo Scientific Escalab 250XI using a monochromated Al Kα X-ray source ($h\nu$ = 1486.6 eV). The pass energy was 30 eV. The Tougaard background was subtracted from the measured spectrum and the peaks were fitted before calculating the d-band center according to previous references.[30−32] The *p* center of the d-band calculation was defined as $\mu_p = \int_{E_F}^{E} N(\varepsilon)\ \varepsilon^p \mathrm{d}\varepsilon$, where $N(\varepsilon)$ was the density of states (DOS), E_F was the Fermi level and *p* was the order of moment.

2.8. X-ray Absorption Near-Edge Structure (XANES) and Extended X-ray Absorption Fine Structure (EXAFS). The X-ray absorption near-edge structure (XANES) and extended X-ray absorption fine structure (EXAFS) spectra were measured at the BL14W1 beamline of the Shanghai Synchrotron Radiation Facility (SSRF). The absorption spectra of the Co K-edge of In_2O_3−Co_3O_4 sample and reference Co_3O_4 were recorded at room temperature in transmission mode. A Si (111) double-crystal monochromator was used to reduce the harmonic content of the monochrome beam. The back-subtracted EXAFS function was converted into *k* space and weighted by k^3 in order to compensate for the diminishing amplitude due to the decay of the photoelectron wave. The Fourier transforming of the k^3-weighted EXAFS data was performed in the range of $k = 3.0$ to 12.8 A^{-1} with a Hanning function window.

2.9. Diffuse Reflectance Infrared Fourier Transform (DRIFT). Diffuse reflectance infrared Fourier transform (DRIFT) spectroscopy of CO adsorbed on the catalysts was measured on a Nicolet Nexus 6700 spectrometer equipped with a MCT detector and a low-temperature sample cell which was fitted with ZnSe windows. The DRIFT spectra obtained were collected in Kubelka−Munk unit with a resolution of 4 cm^{-1} and 64 scans. In situ DRIFT spectra during the CO oxidation at −70 °C at different reaction time were obtained in the flow of 1 vol % CO, 20 vol % O_2 and N_2. The samples were first pretreated at 350 °C for 40 min by the mixed gas of 20 vol % O_2/N_2 before collecting DRIFT spectra.

2.10. Kinetic Data Measurements. The reaction rate was measured at −75 °C under reaction condition of 2 vol % CO, 10 vol % O_2 and N_2. The space-velocity was 600 000 mL/g·h. TOF values were calculated on the basis of the BET surface area. Reaction orders of O_2 and CO were measured in the temperature range of −55 to −95 °C and space velocity of 40 000−600 000 mL/g·h with feed steams of 0.5−2 vol % CO and 5−20 vol % O_2 balanced with N_2. The CO conversion was adjusted to below 15% by varying space velocity so as to eliminate the thermal effect and diffusion effect before calculating the reaction rates.

3. RESULTS AND DISCUSSION

3.1. Catalytic Performance. Figure 1 exhibited the catalytic activity of different catalysts under the condition of 20 vol % O_2, 1 vol % CO, and N_2 balanced in the dry feed gas, and the space-velocity was 15 000 mL/h·g_{cat}. The lowest temperature of complete conversion (LTCC) for CO and TOF values were listed in Table 1. Pure In_2O_3 did not show any detectable catalytic activity in the temperature range of −70 to 0 °C. However, the doping of In_2O_3 significantly enhanced catalytic activity of Co_3O_4. The activities of In_2O_3−Co_3O_4 increased with an increase in In_2O_3 content in the form of a volcano curve, with T_{100} shown in the inset picture of Figure 1. The 25InCo showed the highest activity for CO oxidation. LTCC was as low as −105 °C, whereas it was only −40 °C over pure Co_3O_4. Meanwhile, 25InCo exhibited the highest reaction rate and TOF value for CO oxidation at −75 °C was 1.7 × 10^{-7} mol/s·m^2, which was 5.3 times that on pure Co_3O_4.

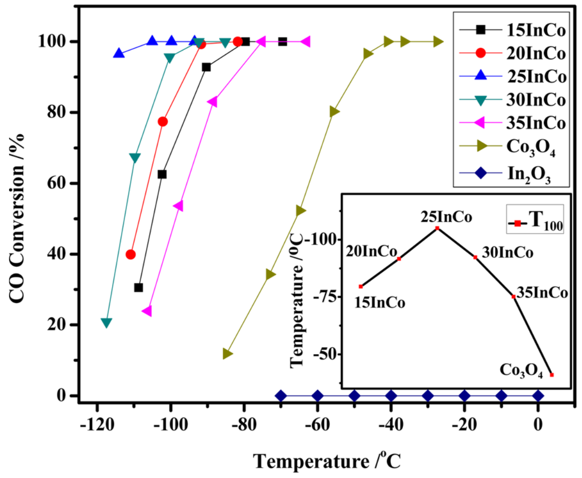

Figure 1. Catalytic activity of Co_3O_4 and In_2O_3−Co_3O_4 samples with different In_2O_3 contents. Inset: the lowest temperature of complete conversion of CO, T_{100} vs In_2O_3 contents.

3.2. Structural Parameters. *3.2.1. X-ray Diffraction.* The XRD patterns of pure Co_3O_4 and In_2O_3−Co_3O_4 samples are shown in Figure 2, and the detailed cell parameters of In_2O_3−Co_3O_4 samples are listed in Table 1. For all In_2O_3−Co_3O_4 samples, the diffraction peaks of In_2O_3 could not be detected. Compared with pure Co_3O_4, the diffraction peaks of Co_3O_4 in In_2O_3−Co_3O_4 catalysts shifted to lower degrees and became broadened, which suggested that the In_2O_3 entered the lattice of Co_3O_4 and resulted in the expansion of lattice due to the larger ionic radius of In^{3+}. However, there was no further shift to a lower degree when the contents of In_2O_3 were higher than 25 wt %, which indicated only appropriate In_2O_3 could be accommodated in the unit cell of Co_3O_4, and the excessive In_2O_3 might be highly dispersed on the surface of Co_3O_4. Meanwhile, the crystallite size of In_2O_3−Co_3O_4 was smaller than that of pure Co_3O_4 (10.7 nm) calculated from the Scherrer Equation, which implied the expansion of Co_3O_4 lattice and surface In_2O_3 suppressed the crystal growth of Co_3O_4. The lattice expansion might alter the original electronic and geometric structure of Co_3O_4.

3.2.2. Raman. For the pure Co_3O_4, there were five Raman-activated modes.[33−35] As shown in Figure 3, the band at 678 cm^{-1} was attributed to the characteristics of octahedral sites (CoO_6), which corresponded to the A_{1g} species in the O_h^7 spectroscopic symmetry. The Raman bands with medium intensity located at 477 and 521 cm^{-1} had E_g and F_{2g}^2 symmetry, respectively. The weak band located at 613 cm^{-1} had the F_{2g}^2 symmetry. The band at 190 cm^{-1} was attributed to the characteristics of tetrahedral sites (CoO_4), which was assigned to the F_{2g}^1 symmetry. The structure of Co_3O_4 showed that the Co^{3+} species were filled in octahedral sites (16a Wyckoff sites), and Co^{2+} species were tetrahedral sites (8a Wyckoff sites).[18] Therefore, the bands at 678 and 190 cm^{-1} could be ascribed to Raman vibration of Co^{3+}-O^{2-} and Co^{2+}-O^{2-}, respectively.

Compared with Co_3O_4, the Raman peaks of In_2O_3−Co_3O_4 samples, especially for the peaks of octahedral sites (CoO_6), shifted to lower frequencies. Our previous research showed that the doped In^{3+} mainly replaced Co^{3+} and entered the octahedral sites,[28] which brought more significant effects of the symmetry of octahedral sites (CoO_6) than that of tetrahedral sites (CoO_4). Correspondingly, the Raman shift of octahedral sites (CoO_6) was more obvious than that of tetrahedral sites (CoO_4). The changes of Raman symmetry indicated that the original coordinative environment of tetrahedral and octahedral structure had been changed due to the doping of In_2O_3, which was assigned to the lattice distortion or residual stress of the spinel structure.[35] Hence, we could conclude that the doping of In_2O_3 produced structural defects and lattice distortion, which was suggested to be favorable for the formation of oxygen vacancy and weakening the bond strength of Co−O.

3.2.3. UV−vis Absorption Spectroscopy. The UV−vis spectra of Co_3O_4 and In_2O_3−Co_3O_4 in Figure 4 showed two absorption bands centered at about 410 and 690 nm, which were assigned to the ligand-to-metal charge transfer from O^{2-} to Co^{2+} (basic optical band gap energy, or valence to conduction band excitation) and O^{2-} to Co^{3+} (Co^{3+} level located below the conduction band), respectively.[36−38] For the In_2O_3−Co_3O_4, the absorption edge shifted to lower energy compared with that of pure Co_3O_4. Especially for the In_2O_3−Co_3O_4 with higher In_2O_3 contents, the red shift of absorption

Table 1. Reaction Rate, TOF Values, and Structural Parameters of Co_3O_4 and $In_2O_3-Co_3O_4$ Samples

sample	LTCC (°C)	reaction rate (10^{-6} mol/g·s)[a]	BET surface area (m^2/g)	TOF value (10^{-8} mol/s·m^2)[b]	cell constant (a_0 /Å)	crystal size (d/nm)[c]
Co_3O_4	−40	3.89	121.6	3.2	8.075	10.7
15InCo	−80	8.07	100.1	8.1	8.088	8.4
20InCo	−92	11.43	97.2	11.8	8.093	8.6
25InCo	−105	15.42	90.8	17.0	8.100	8.8
30InCo	−92	13.11	83.6	15.7	8.099	7.0
35InCo	−75	6.21	80.2	7.7	8.091	7.1

[a] Reaction rate was measured at −75 °C under reaction condition of 2 vol % CO, 10 vol % O_2, and N_2 balance with SV = 600 000 mL/g·h. [b] TOF values were calculated on the basis of the BET surface area and not on the number of surface active sites. [c] The crystal size was calculated through the FMWH of (311) peak using the Scherrer Equation

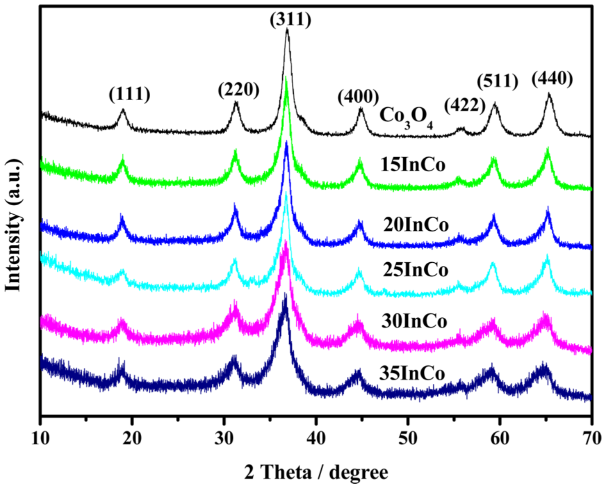

Figure 2. XRD patterns of pure Co_3O_4 and $In_2O_3-Co_3O_4$ samples.

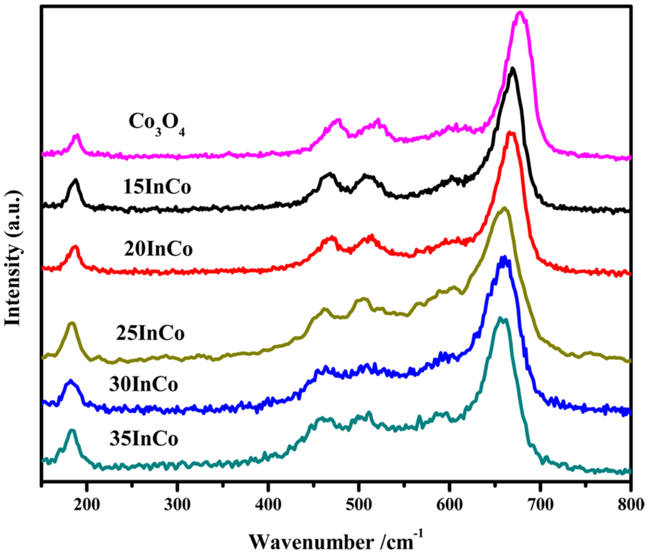

Figure 3. Raman spectra of pure Co_3O_4 and $In_2O_3-Co_3O_4$ samples.

edge became much more obvious, which indicated the doping of In_2O_3 significantly decreased the band gap and promoted the electron transition from the highest occupied molecular orbital (HOMO, at the top of the valence band) to the lowest unoccupied molecular orbital (LUMO, at the bottom of the conduction band). For the redox reaction cycle, the electron transfer was normally involved in the transit of exciting electrons from the HOMO to LUMO,[39] the break of weaker metal−oxygen bonds required lower energy according to the theory of Chen[40] and Iglesia.[41] Hence, the red shift of the absorption edge indicated the doping of In_2O_3, weakened the bond energy of Co−O bonds, and made the extraction of O easier from the surface of Co_3O_4.

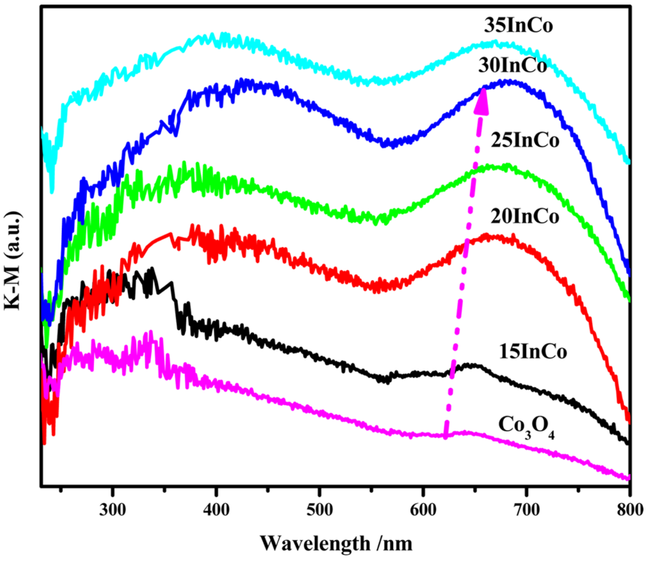

Figure 4. UV−vis spectra of Co_3O_4 and $In_2O_3-Co_3O_4$ samples.

3.3. Redox Ability. *3.3.1. H_2-TPR and O_2-TPD.* The low-temperature H_2-TPR profiles of pure Co_3O_4 and $In_2O_3-Co_3O_4$ samples were shown in Figure 5. For the pure Co_3O_4 sample, an obvious reduction peak at −67 °C was detected. After the doping of In_2O_3, the reduction peak shifted to lower temperature. Among them, 25InCo showed the lowest reduction temperature. With a continuous increase in In_2O_3 content to 30%, the reduction peak slightly shifted to higher temperature. These results showed that the doping of In_2O_3 significantly accelerated the extraction of surface lattice oxygen species, which corresponded to the relaxation of the surface Co−O bond.

To investigate the interaction between the adsorbed oxygen species and Co_3O_4 surface, O_2-TPD experiments were carried out over pure Co_3O_4 and 25InCo starting from −80 to 0 °C. In Figure 6, there was an obvious desorption peak at −60 °C on pure Co_3O_4 and at around −70 °C on the 25InCo samples, which could be assigned to the desorption of surface oxygen species adsorbed on oxygen vacancy.[13] The shift of O_2 desorption peak to lower temperature over 25InCo indicated that the adsorbed oxygen on 25InCo was more easily desorbed, which implied the activation of surface adsorbed oxygen was

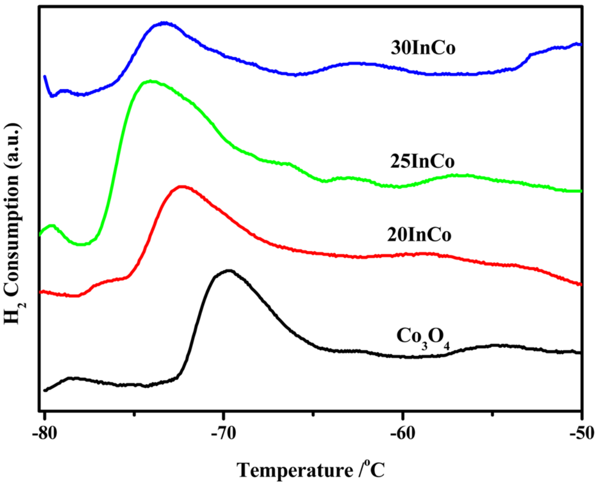

Figure 5. Low-temperature H_2-TPR profiles of pure Co_3O_4 and $In_2O_3-Co_3O_4$ samples.

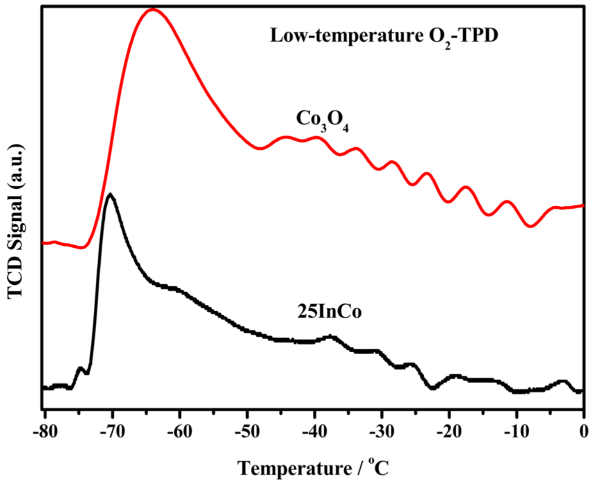

Figure 6. Low-temperature O_2-TPD profiles of pure Co_3O_4 and 25InCo samples.

promoted. Meanwhile, the calculated amount of O_2 desorption by Co_3O_4 weight exhibited O_2 desorption amount of 25InCo was higher by 7.2% than that of pure Co_3O_4, which indicated that the doping of In facilitated the formation of oxygen vacancy. This result was in line with our previous DFT results,[28] which showed the formation energy of oxygen vacancy decreased after the doping of In_2O_3.

Because O_2 activation was an important factor for CO oxidation of Co_3O_4,[11−14] the enhanced ability for providing active oxygen species would promote the surface reaction, which was in accord with the results of activation energy shown in Table 2. Hence, the promotion of the O_2 activation should be one reason for the outstanding catalytic performance of $In_2O_3-Co_3O_4$ samples for CO oxidation.

3.4. Electronic Structure.

3.4.1. X-ray Absorption Spectroscopy. The Co_3O_4 had a spinel structure containing Co^{3+} in an octahedral coordination and Co^{2+} in a tetrahedral coordination.[18] According to the refs 42−45, the first peak represented that Co (Co^{2+}) was tetrahedrally coordinated by 1.33 O at 1.81 Å, and Co (Co^{3+}) was octahedrally coordinated by 4 O at 1.99 Å. These two shells were too close to be separated in the radial structure functions (RSFs), so they were taken as the first shell. The second and third peaks corresponded to the Co−Co coordination shell at 2.87 Å (coordination number, CN: 4) and 3.35 Å (CN: 8), and the fourth peak should be attributed to the higher Co−Co and Co−O shells. Therefore, in Figure 7a, the peaks in the RSF of Co_3O_4 at 1.47, 2.42, 3.00, and 4.63 Å (not corrected by phase scattering shift), could be assigned to the above four coordination shells. It was very clear that all the $In_2O_3-Co_3O_4$ samples displayed the almost identical coordination peaks as that of Co_3O_4, which indicated that $In_2O_3-Co_3O_4$ still kept similar coordinative structure with Co_3O_4 as shown in Table 3. But the decrease of high coordination peaks intensity indicated that the presence of disorder in the structure of $In_2O_3-Co_3O_4$ samples,[42,45] which was in accord with the Raman results that doping of In_2O_3 produced more structural defects and lattice distortion. Meanwhile, the bond distance of Co−O was slightly elongated from 1.91 Å in pure Co_3O_4 to 1.93 Å in the 25InCo, which indicated the lattice expansion and the relaxation of Co−O bond in the $In_2O_3-Co_3O_4$.

The changes in the electronic structure of cobalt occurring through the doping of In_2O_3 were investigated by the XANES at the Co K-edge. The changes of both main absorption edge position and white line intensity was in the form of an inverse volcano with the increase in In_2O_3 content, as shown in Figure 7b,c. The decrease in the white line intensity suggested that the density of unoccupied d states and the oxidation states of the absorber atom were lower,[46−48] which might be due to the downshift of d orbital of electronic states.[49,50]

As shown in Figure 7d, the pre-edge of Co K edge was corresponding to the transition of electron from 1s to 3d.[51,52] The shift of pre-edge position to lower energy showed that the d-band center was pulled down, which was induced by less empty antibonding states.[50] Therefore, the adsorption strength of CO would become weaker on the surface of $In_2O_3-Co_3O_4$ samples.[53,54]

3.4.2. X-ray Photoelectron Spectroscopy. The XPS characterization was performed to investigate the surface chemical state of the catalysts, as shown in Figure 8. The peaks of Co^{3+} and Co^{2+} were fitted according to refs 29,38. The binding energies (BE) of Co^{2+} and Co^{3+} on the surface of $In_2O_3-Co_3O_4$ were shifted to lower BE compared with that of pure Co_3O_4, as shown in Table 4. Furthermore, the shift of BE was in the form of a volcano with the doping of In_2O_3, which showed the modification on electronic structure of Co_3O_4 was dependent on the content of In_2O_3. The BE of In 3d in the $In_2O_3-Co_3O_4$ samples did not show obvious changes with the doping of In_2O_3. Two peaks at 452.1 and 444.6 eV for $3d_{3/2}$

Table 2. Apparent Activation Energy and Reaction Order of CO Oxidation over Pure Co_3O_4 and $In_2O_3-Co_3O_4$ Samples

sample	Co_3O_4	15InCo	20InCo	25InCo	30InCo	35InCo
Ea (kJ/mol)	20.1	15.1	15.2	14.6	15.5	15.1
CO reaction order	−0.84	/	/	−0.38	/	/
O_2 reaction order	1.02	/	/	0.74	/	/

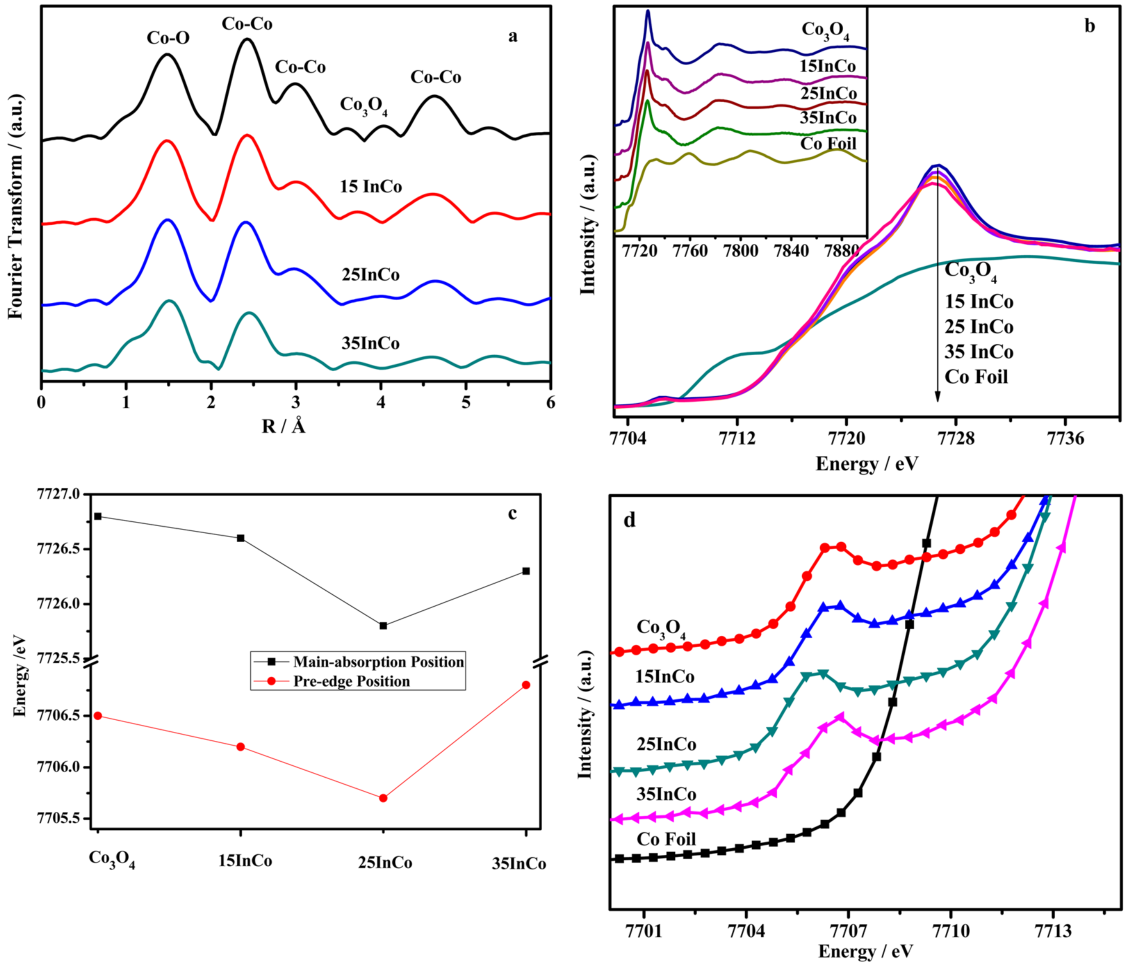

Figure 7. X-ray absorption spectroscopy of Co_3O_4 and In_2O_3−Co_3O_4 samples: k^3-weighted Fourier transforms of the experimental EXAFS spectra at the Co K-edge for Co_3O_4 and In_2O_3−Co_3O_4 samples (a). Normalized XANES spectra at the Co K-edge of Co_3O_4 and In_2O_3−Co_3O_4 samples (b). Scheme of the energy position of pre-edge and main absorption of Co K-edge of Co_3O_4 and In_2O_3−Co_3O_4 samples (c). Pre-edge of XANES spectra at the Co K-edge of Co_3O_4 and In_2O_3−Co_3O_4 samples (d).

Table 3. Results of the EXAFS Analysis at the Co K-edge for the Pure Co_3O_4 and In_2O_3−Co_3O_4 Samples

	R (Å)			R (Å)		
sample	Co−O	N atoms[a]	$2\sigma^2$	Co−Co	N atoms	$2\sigma^2$
Co_3O_4	1.91	5.3	0.0055	2.85	4.0	0.00674
				3.35	8.0	0.01692
15InCo	1.92	4.6	0.0042	2.86	5.3	0.01296
				3.37	6.5	0.01786
25InCo	1.93	4.5	0.0037	2.86	6.0	0.01428
				3.39	4.7	0.01488
35InCo	1.91	5.9	0.0116	2.87	4.3	0.01608
				3.38	3.5	0.02216

[a] Coordination number.

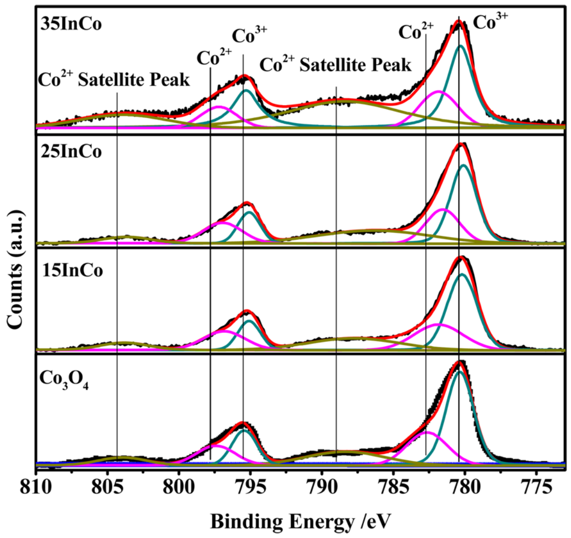

Figure 8. XPS spectra of Pure Co_3O_4 and In_2O_3−Co_3O_4 samples.

and $3d_{5/2}$ were assigned to In^{3+}.[55] Combined with XANES data, it was clear that the oxidation states of Co^{2+} and Co^{3+} were slightly decreased, which indicated lattice oxygen in In_2O_3−Co_3O_4 tended to attract fewer electrons from its adjacent Co cations to balance its excess electrons due to the presence of In^{3+}.

3.4.3. Derivation of d-Band Centers. Nørskov and coworkers proposed a band model based on DFT calculations to describe how the changes in the d-band center affected the adsorption energy over surface.[50,56] The location of the d-band center (ε_d) relative to the Fermi level was considered as an important parameter in determining the ability of the surface to bond to a number of adsorbates.[57] Therefore, the d-band centers of In_2O_3−Co_3O_4 catalysts were calculated according to

Table 4. Binding Energy of Co^{3+} and Co^{2+} in Co_3O_4 and In_2O_3−Co_3O_4 Samples

sample	Co^{3+} BE/eV		Co^{2+} BE/eV		Co^{2+} satellite peak BE/eV	
Co_3O_4	780.4	795.4	782.0	797.4	788.4	803.9
15InCo	780.2	795.2	781.8	797.2	788.3	803.8
25InCo	780.1	795.1	781.6	797.0	788.2	803.7
35InCo	780.3	795.3	781.8	797.2	788.4	803.9

the equation described in refs 30−32,58. Figure 9a shows the XPS valence band results of In_2O_3−Co_3O_4 and pure Co_3O_4. According to previous studies[59,60], the peaks at 1.6 and 2.8 eV could be attributed to the Co 3d of Co^{3+} and Co^{2+}, respectively; the peak at 5.5 eV should be attributed to the O 2p; the peak at 10.4 eV belonged to the Co^{3+} satellite. The XPS valence band results indicated the d-band center of Co_3O_4 shifted further away from the Fermi level after the doping of In_2O_3, which agreed with the XANES results. The change trend of the d-band center was in line with that of the LTCC of In_2O_3−Co_3O_4, as shown in Figure 9b. Lower d-band center energy position corresponded with higher catalytic activity. The correlation between the d-band center and catalytic activity revealed that not only oxygen activation but also CO adsorption strength influenced the catalytic activity.

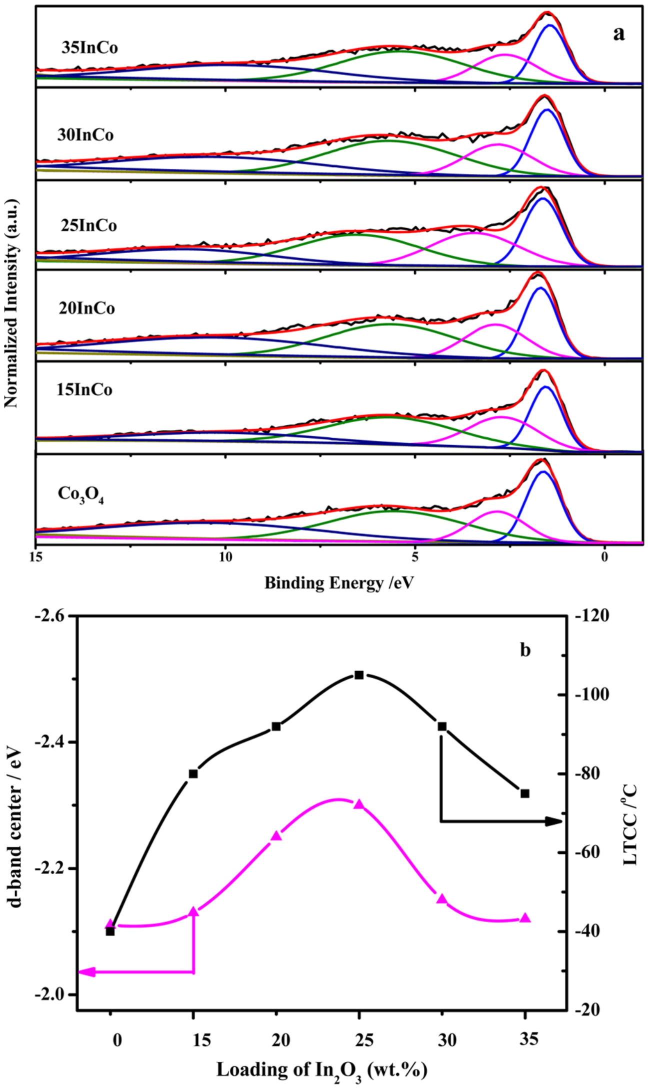

Figure 9. (a) XPS valence band results of In_2O_3−Co_3O_4 and pure Co_3O_4 and (b) curves of d-band center and LTCC vs contents of In_2O_3. The negative value of left *Y*-axis represented the position of d-band center under the Fermi level.

3.5. Accumulation of Surface Carbonate Species. Strong CO_2 adsorption could lead to the severe accumulation of surface carbonate species (ASCS), which has resulted in the deactivation of Co_3O_4 for CO oxidation.[10,14] Therefore, weaker CO adsorption was expected to decrease the adsorption and accumulation of CO_2. As observed by in situ DRIFTS (shown in Figure 10), the ASCS was hardly avoided during the whole reaction processes due to the intrinsic properties of Co_3O_4. But the ASCS observed at −70 °C declined remarkably on the surface of In_2O_3−Co_3O_4 compared with that on the pure Co_3O_4 surface. According to the literature,[8,61,62] the peaks at around 1413 and 1220 cm^{-1} could be ascribed to the formation of unidentate carbonates, which was ascribed to the interaction between carbonate dioxide and the basic sites (coordinatively unsaturated oxygen anions). The peak at around 1630 cm^{-1} was attributed to bicarbonate species. Lower ASCS on the surface of In_2O_3−Co_3O_4 suggested CO adsorption strength was weaker, which was induced by the downshift of d-band center of Co_3O_4. The inhibitory effect on the ASCS helped to maintain the high activity of In_2O_3−Co_3O_4 catalysts for a longer time. Hence, the stability of CO oxidation at 0 °C over 25InCo was promoted greatly to 600 min from 210 min (i.e., that of Co_3O_4).

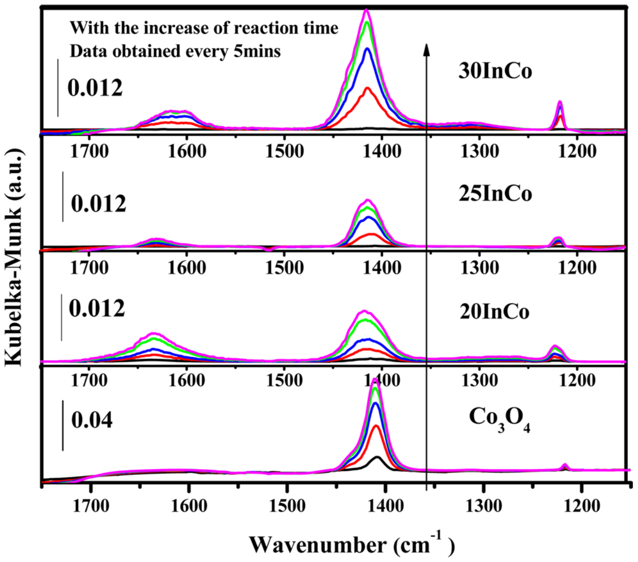

Figure 10. Accumulation of surface carbonate species at −70 °C over In_2O_3−Co_3O_4 and pure Co_3O_4 at different reaction time in the flow of 1 vol % CO, 20 vol % O_2, and N_2 balanced.

4. KINETIC DATA

4.1. Reaction Kinetics of CO Oxidation. The kinetic data was shown in Figure 11a,b. The apparent activation energies were listed in Table 2 for 25InCo and pure Co_3O_4 catalysts. Lower activation energies of In_2O_3−Co_3O_4 indicated that CO oxidation over In_2O_3−Co_3O_4 was much easier than that over the pure Co_3O_4 surface. The reaction orders of CO and O_2 were −0.38 and 0.74 over the 25InCo catalyst and −0.64 and 0.88 over pure Co_3O_4, as shown in Table 2. The increase of CO

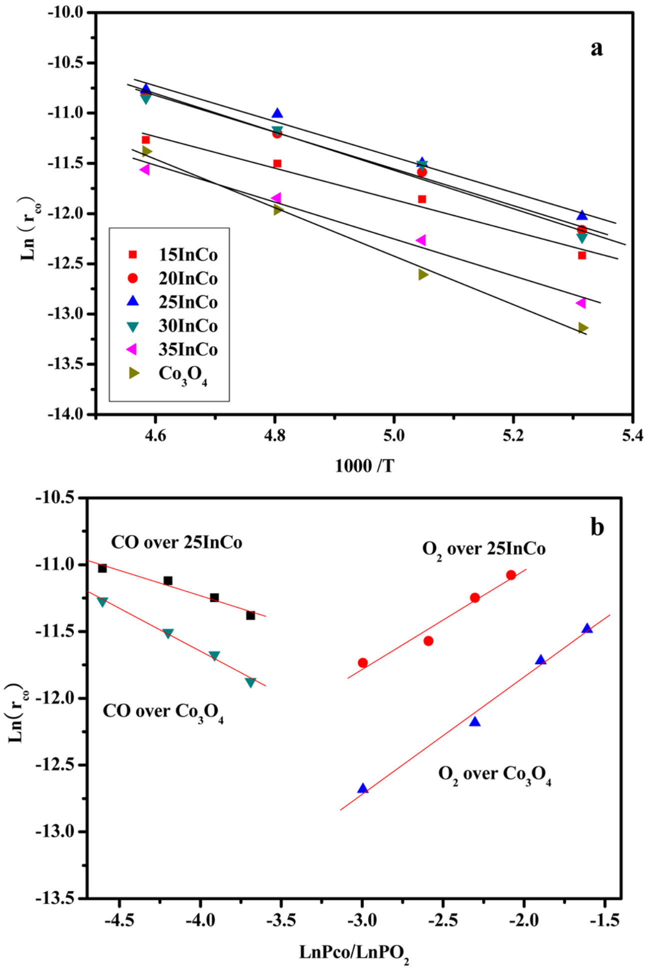

Figure 11. Reaction kinetics of CO oxidation: (a) apparent activation energy of CO oxidation over pure Co_3O_4 and In_2O_3−Co_3O_4 samples; (b) reaction order of pure Co_3O_4 and 25InCo.

reaction order on 25InCo indicated a decrease in adsorption strength of CO, because the negative reaction order indicated the surface was saturated by the reactants.[63] Furthermore, the decrease in O_2 reaction order indicated that the process of O_2 adsorption and activation over 25InCo was more efficient than that of pure Co_3O_4.

5. DISCUSSION

For CO oxidation on supported noble metal (NM) catalysts, both CO adsorption and O_2 adsorption and activation were on NM; therefore, the competitive adsorption between CO and O_2 determined the catalytic activity of NM. For example, appropriate CO and O_2 adsorption energies made nanogold catalysts exhibit the maximum Sabatier rate at low temperature.[64] However, for the CO oxidation on TMOs, CO usually adsorbed on the cationic metal sites, and the CO oxidation reaction mechanism followed the Mars−van Krevelen mechanism,[15,27,65−67] which suggested that simultaneously tuning the activity of lattice oxygen and CO adsorption should be an efficient method to design novel catalysts.

For the enhancement of oxygen activity on TMOs, an efficient way was to weaken the M−O bond by elongating the length of the M−O bond and increasing oxygen vacancy and/or reducing the chemical valence of metal ions. The most common method to meet this subject was choosing a suitable doping cation. For example, the dopant (M′) with larger ionic radius and weaker M′−O bonding strength could expand the lattice constant of TMOs and create a structural defect and residual stress as well as easily produce oxygen vacancy, which could promote the activation of lattice oxygen and enhance the adsorption of oxygen. In fact, M−O bond strength and M chemical state in TMOs could be simultaneously tuned, which depended on the properties of doped M′.

For In_2O_3, the ionic radius of In^{3+} was larger than that of Co^{3+}, and bonding energy of In−O was lower than that of Co−O. After the doping of In_2O_3, the bond length of Co−O was elongated, which was confirmed by results of XRD and EXAFS. The red-shift of UV−vis absorption showed that the electron transfer from O^{2-} to Co^{3+} and/or Co^{2+} in In_2O_3−Co_3O_4 was easier than that in pure Co_3O_4.[35] XPS spectra also revealed that the presence of In_2O_3 decreased the oxidation states of Co^{3+} and Co^{2+}. All of these results suggested that the doping of In_2O_3 not only decreased the oxidation states of Co^{3+}/Co^{2+} but also weakened the bond strength of Co−O. As expected, the doping of In_2O_3 significantly promoted the activity of lattice oxygen, which was confirmed by H_2-TPR results.

Except the adsorption and activation of O_2, CO adsorption was always emphasized in CO oxidation, because good ability of CO adsorption could provide enough surface adsorbed CO species, which was necessary for CO oxidation based on the common Mars−van Krevelen mechanism. It should be noted that CO adsorption ability should contain adsorption amount and adsorption strength. Normally increasing CO adsorption strength could increase adsorption amount of CO. However, too strong CO adsorption strength could increase the reaction barrier of CO reacting with active oxygen and block the desorption of CO_2, which led to the accumulation of surface carbonate species and severely impaired the catalytic activity for metal oxide catalysts.[10,14,27]

Therefore, under the premise of enough CO adsorption, decreasing CO adsorption strength could promote CO oxidation on TMOs. Co^{3+} in Co_3O_4, as active species in CO oxidation, had strong ability for CO adsorption.[10,14,27] For CO oxidation at the reaction temperature of −115 ∼ −40 °C, the adsorption energy of CO should be higher than 0.32 eV (S (the entropy of CO) = 197.66 J·K^{-1}·mol^{-1}, T = 158.15−233.15 K, TS = 0.32−0.48 eV). Our calculated results showed that CO adsorption energy was 1.16 eV on pure Co_3O_4 (100)-B.[28] Therefore, appropriate CO adsorption strength on Co_3O_4-based catalyst could not only decrease the reaction barrier but also accelerate the CO_2 desorption.

CO adsorption strength depended on the intrinsic properties of cationic metal.[64,68−70] Several methods could be used to decrease the CO adsorption strength, such as decreasing the particle size,[69,70] decreasing the oxidation states, and downshifting the d-band center.[56,57] The doping of In_2O_3 not only decreased the oxidation state but also downshifted the d band center of Co^{3+}/Co^{2+}. As confirmed by XANES and XPS valence band, the doping of In_2O_3 made the d-band center of Co downshifted, in the form of volcano curve with the increase of In_2O_3 loadings, which decreased the adsorption strength of CO. The decrease of CO adsorption strength significantly weakened the adsorption and accumulation of CO_2, which was confirmed by in situ DRIFT results of the ASCS.

Combined with the above discussion, we could tune the O_2 activation and CO adsorption over Co_3O_4 simultaneously through the choice of suitable dopant. Doping cations with larger ionic radius and lower M−O bonding energy could promote the catalytic performance of Co_3O_4 for CO oxidation. In_2O_3 met these requirements and significantly promoted CO oxidation as expected.

6. CONCLUSIONS

For CO oxidation over the NM or TMO catalysts, the adsorption strength of CO and O_2 activation should be equally considered if the excellent catalytic activity was desired. Here, we presented a new strategy to design novel and efficient Co_3O_4 catalyst for CO oxidation through doping appropriate heteroatom to modify the electronic structure of Co_3O_4, which enhanced the O_2 activation and weakened the adsorption strength of CO simultaneously.

The doping of In cations caused the expansion of unit cell, structural defects and modified the electronic structure of Co_3O_4. On the one hand, the geometric changes weakened the bond strength of Co−O and elongated the bond length of Co−O, which promoted the formation of oxygen vacancy and enhanced the redox ability, and therefore the surface reaction became much easier. On the other hand, the modification on the surface electronic structure made the d-band center downshifted, which significantly weakened the adsorption strength of CO. The weaker adsorption strength of CO lowered the reaction barrier and inhibited the accumulation of surface carbonate species. Therefore, simultaneously tuning on the CO adsorption and O_2 activation through doping appropriate In_2O_3 greatly promoted the catalytic activity and stability of Co_3O_4 for CO oxidation at low temperature.

■ AUTHOR INFORMATION

Corresponding Authors

*E-mail: yunguo@ecust.edu.cn. Tel.: (+) 86-21-64253703.
*E-mail: gzhlu@ecust.edu.cn.

Author Contributions

[†]Y.L. and J.M. contributed equally to this work.

Notes

The authors declare no competing financial interest.

■ ACKNOWLEDGMENTS

This project was supported financially by the National Basic Research Program of China (2010CB732300, 2013CB933201), the National High Technology Research and Development Program of China (2012AA062703, 2012AA111717), NSFC of China (21171055, 21273150, 21333003, 21303051), and the "Shu Guang" Project of the Shanghai Municipal Education Commission. The authors thank the National Supercomputer Center in Jinan for computing time. P.H. thanks the Chinese Government for the "Thousands Talents" program.

■ REFERENCES

(1) Carabineiro, S. A. C.; Machado, B. F.; Bacsab, R. R.; Serpb, P.; Dražić, G.; Faria, J. L.; Figueiredo, J. L. *J. Catal.* **2010**, *273*, 191−198.
(2) Li, S. Y.; Liu, G.; Lian, H. L.; Jia, M. J.; Zhao, G. M.; Jiang, D. Z.; Zhang, W. X. *Catal. Commun.* **2008**, *9*, 1045−1049.
(3) Haruta, M.; Kobayashi, T.; Yamada, N. *Chem. Lett.* **1987**, *16*, 405−408.
(4) Chen, M. S.; Goodman, D. W. *Science* **2004**, *306*, 252−255.
(5) Qiao, B. T.; Liu, L. Q.; Zhang, J.; Deng, Y. Q. *J. Catal.* **2009**, *261*, 241−244.
(6) Lou, Y.; Wang, L.; Zhang, Y. H.; Zhao, Z. Y.; Zhang, Z. G.; Lu, G. Z.; Guo, Y. *Catal. Today* **2011**, *175*, 610−614.
(7) Cunningham, D. A. H.; Kobayashi, T.; Kamijo, N.; Haruta, M. *Catal. Lett.* **1994**, *25*, 257−264.
(8) Grillo, F.; Natile, M. M.; Glisenti, A. *Appl. Catal., B* **2004**, *48*, 267−274.
(9) Thormählen, P.; Skoglundh, M.; Fridell, E.; Andersson, B. *J. Catal.* **1999**, *188*, 300−310.
(10) Xie, X. W.; Li, Y.; Liu, Z. Q.; Haruta, M.; Shen, W. J. *Nature* **2009**, *458*, 746−749.
(11) Jansson, J.; Palmqvist, A. E. C.; Fridell, E.; Skoglundh, M.; Österlund, L.; Thormählen, P.; Langer, V. *J. Catal.* **2002**, *211*, 387−397.
(12) Jansson, J. *J. Catal.* **2000**, *194*, 55−60.
(13) Yu, Y. B.; Takei, T.; Ohashi, H.; He, H.; Zhang, X. L.; Haruta, M. *J. Catal.* **2009**, *267*, 121−128.
(14) Wang, H. F.; Kavanagh, R.; Guo, Y. L.; Guo, Y.; Lu, G. Z.; Hu, P. *Angew. Chem., Int. Ed.* **2012**, *51*, 6657−6661.
(15) Broqvist, P.; Panas, I.; Persson, H. *J. Catal.* **2002**, *210*, 198−206.
(16) Kunz, S.; Schweinberger, F. F.; Habibpour, V.; Röttgen, M.; Harding, C.; Arenz, M.; Heiz, U. *J. Phys. Chem. C* **2010**, *114*, 1651−1654.
(17) Pollard, M. J.; Weinstock, B. A.; Bitterwolf, T. E.; Griffiths, P. R.; Newbery, A. P.; Paine, J. B. *J. Catal.* **2008**, *254*, 218−225.
(18) Cabanas, M. C.; Binotto, G.; Larcher, D.; Lecup, A.; Giordani, V.; Tarascon, J. M. *Chem. Mater.* **2009**, *21*, 1939−1947.
(19) Tang, X. F.; Li, J. H.; Hao, J. M. *Mater. Res. Bull.* **2008**, *43*, 2912−2918.
(20) Hu, L. H.; Sun, K. Q.; Peng, Q.; Xu, B. Q.; Li, Y. D. *Nano Res.* **2010**, *3*, 363−368.
(21) Jia, C. J.; Schwickardi, M.; Weidenthaler, C.; Schmidt, W.; Korhonen, S.; Weckhuysen, B. M.; Schüth, F. *J. Am. Chem. Soc.* **2011**, *133*, 11279−11288.
(22) Widmann, D.; Leppelt, R.; Behm, R. J. *J. Catal.* **2007**, *251*, 437−442.
(23) Tüysüz, H.; Comotti, M.; Schüth, F. *Chem. Commun.* **2008**, 4022−4024.
(24) Wang, Y. Z.; Zhao, Y. X.; Gao, C. G.; Liu, D. S. *Catal. Lett.* **2008**, *125*, 134−138.
(25) Lou, Y.; Wang, L.; Zhao, Z. Y.; Zhang, Y. H.; Zhang, Z. G.; Lu, G. Z.; Guo, Y.; Guo, Y. L. *Appl. Catal., B* **2014**, *146*, 43−49.
(26) Liu, Z. P.; Hu, P. *J. Chem. Phys.* **2001**, *115*, 4977−4980.
(27) Wang, H. F.; Kavanagh, R.; Guo, Y. L.; Guo, Y.; Lu, G. Z.; Hu, P. *J. Catal.* **2012**, *296*, 110−119.
(28) Lou, Y.; Cao, X. M.; Lan, J. G.; Wang, L.; Dai, Q. G.; Guo, Y.; Ma, J.; Zhao, Z. Y.; Hu, P.; Lu, G. Z. *Chem. Commun.* **2014**, *50*, 6835−6838.
(29) Deng, J. G.; Zhang, L.; Dai, H. X.; He, H.; Au, C. T. *Catal. Lett.* **2008**, *123*, 294−300.
(30) Stamenkovic, V. R.; Mun, B. S.; Arenz, M.; Mayrhofer, K. J.; Lucas, C. A.; Wang, G.; Ross, P. N.; Markovic, N. M. *Nat. Mater.* **2007**, *6*, 241−247.
(31) Mun, B. S.; Watanabe, M.; Rossi, M.; Stamenkovic, V.; Markovic, N. M.; Ross, P. N. *J. Chem. Phys.* **2005**, *123*, 204717.
(32) Hofmann, T.; Yu, T. H.; Folse, M.; Weinhardt, L.; Bär, M.; Zhang, Y. F.; Merinov, B. V.; Myers, D. J.; Goddard, W. A.; Heske, C. *J. Phys. Chem. C* **2012**, *116*, 24016−24026.
(33) He, L.; Li, Z. C.; Zhang, Z. J. *Nanotechnology* **2008**, *19*, 155606.
(34) Liu, Q.; Wang, L. C.; Chen, M.; Cao, Y.; He, H. Y.; Fan, K. N. *J. Catal.* **2009**, *263*, 104−113.
(35) Lopes, I.; Hassan, N. E.; Guerba, H.; Wallez, G.; Davidson, A. *Chem. Mater.* **2006**, *18*, 5826−5828.
(36) Shi, W.; Chopra, N. *ACS Appl. Mater. Interfaces* **2012**, *4*, 5590−5607.
(37) Zhang, Y. G.; Chen, Y. C.; Wang, T.; Zhou, J. H.; Zhao, Y. G. *Microporous Mesoporous Mater.* **2008**, *114*, 257−261.
(38) Xu, R.; Zeng, H. C. *Langmuir* **2004**, *20*, 9780−9790.
(39) Acerbi, N.; Edman Tsang, S. C.; Jones, G.; Golunski, S.; Collier, P. *Angew. Chem., Int. Ed.* **2013**, *52*, 7737−7741.
(40) Mihai, O.; Chen, D.; Holmen, A. *J. Catal.* **2012**, *293*, 175−185.
(41) Weiss, B. M.; Iglesia, E. *J. Catal.* **2010**, *272*, 74−81.
(42) Luo, J. Y.; Meng, M.; Li, X.; Li, X. G.; Zha, Y. Q.; Hu, T. D.; Xie, Y. N.; Zhang, J. *J. Catal.* **2008**, *254*, 310−324.

(43) Huffman, G. P.; Shah, N.; Zhao, J. M.; Huggins, F. E.; Hoost, T. E.; Halvorsen, S.; Goodwin, J. G. *J. Catal.* **1995**, *151*, 17−25.

(44) Luo, J. Y.; Meng, M.; Qian, Y.; Zou, Z. Q.; Xie, Y. N.; Hu, T. D.; Liu, T.; Zhang, J. *Catal. Lett.* **2007**, *116*, 50−56.

(45) Morales, F.; Grandjean, D.; Mens, A.; Groot, F. M. F. d.; Weckhuysen, B. M. *J. Phys. Chem. B* **2006**, *110*, 8626−8639.

(46) Erickson, E. M.; Thorum, M. S.; Vasic, R.; Marinkovic, N. S.; Frenkel, A. I.; Gewirth, A. A.; Nuzzo, R. G. *J. Am. Chem. Soc.* **2012**, *134*, 197−200.

(47) Russell, A. E.; Rose, A. *Chem. Rev.* **2004**, *104*, 4613−4635.

(48) Kirby, J. A.; Goodin, D. B.; Wydrzynski, T.; Robertson, A. S.; Klein, M. P. *J. Am. Chem. Soc.* **1981**, *103*, 5537−5542.

(49) Hu, P.; Huang, Z.; Amghouz, Z.; Makkee, M.; Xu, F.; Kapteijn, F.; Dikhtiarenko, A.; Chen, Y.; Gu, X.; Tang, X. *Angew. Chem., Int. Ed.* **2014**, *53*, 3418−3421.

(50) Ruban, A.; Hammer, B.; Stoltze, P.; Skriver, H. L.; Nørskov, J. K. *J. Mol. Catal. A* **1997**, *115*, 421−429.

(51) Ellis, T.; Jiang, D. E. *J. Mater. Res.* **1996**, *11*, 2242−2256.

(52) Bai, L. G.; Pravica, M.; Zhao, Y. S.; Park, C. Y.; Meng, Y.; Sinogeikin, S. V.; Shen, G. Y. *J. Phys.: Condens. Matter.* **2012**, *24*, 435401.

(53) Gan, L. Y.; Zhao, Y. J. *J. Chem. Phys.* **2010**, *133*, 094703.

(54) Kitchin, J. R.; Nørskov, J. K.; Barteau, M. A.; Chen, J. G. *J. Chem. Phys.* **2004**, *120*, 10240−10246.

(55) Meng, X. Q.; Tang, L. M.; Li, J. B. *J. Phys. Chem. C* **2010**, *114*, 17569−17573.

(56) Hammer, B.; Nørskov, J. K. *Adv. Catal.* **2000**, *45*, 71−129.

(57) Holloway, S.; Lundqvist, B. I.; Nørskov, J. K. *Proceedings of the 8th International Congress on Catalysis*, Berlin (West), Germany, July 2−6, 1984; Vol. *4*, pp 85−95.

(58) Hua, S. Z.; Scudiero, L.; Ha, S. *Electrochim. Acta* **2012**, *83*, 354−358.

(59) Hiifner, G. K.; Wertheim, S. *Phys. Rev. Lett.* **1972**, *28*, 1028−1031.

(60) Qiao, L.; Xiao, H. Y.; Meyer, H. M.; Sun, J. N.; Rouleau, C. M.; Puretzky, A. A.; Geohegan, D. B.; Ivanov, I. N.; Yoon, M.; Weber, W. J.; Biegalski, M. D. *J. Mater. Chem. C* **2013**, *1*, 4628−4633.

(61) Gatehouse, B. M.; Livingstone, S. E.; Nyholm, R. S. *J. Chem. Soc.* **1958**, 3137−3142.

(62) Jansson, J.; Skoglundh, M.; Fridell, E.; Thormählen, P. *Top. Catal.* **2001**, *16/17*, 385−389.

(63) Phatak, A. A.; Koryabkina, N.; Rai, S.; Ratts, J. L.; Ruettinger, W.; Farrauto, R. J.; Blau, G. E.; Delgass, W. N.; Ribeiro, F. H. *Catal. Today* **2007**, *123*, 224−234.

(64) Falsig, H.; Hvolbæk, B.; Kristensen, I. S.; Jiang, T.; Bligaard, T.; Christensen, C. H.; Nørskov, J. K. *Angew. Chem., Int. Ed.* **2008**, *47*, 4835−4839.

(65) Kim, H. Y.; Henkelman, G. *J. Phys. Chem. Lett.* **2013**, *4*, 216−221.

(66) Ramesh, K.; Chen, L. W.; Chen, F. X.; Liu, Y.; Wang, Z.; Han, Y. F. *Catal. Today* **2008**, *131*, 477−482.

(67) Maciejewski, M.; Fabrizioli, P.; Grunwaldt, J. D.; Sven Becker, O.; Baiker, A. *Phys. Chem. Chem. Phys.* **2001**, *3*, 3846−3855.

(68) Lopez, N.; Janssens, T. V. W.; Clausen, B. S.; Xu, Y.; Mavrikakis, M.; Bligaard, T.; Nørskov, J. K. *J. Catal.* **2004**, *223*, 232−235.

(69) Moses-DeBusk, M.; Yoon, M.; Allard, L. F.; Mullins, D. R.; Wu, Z.; Yang, X.; Veith, G.; Stocks, G. M.; Narula, C. K. *J. Am. Chem. Soc.* **2013**, *135*, 12634−12645.

(70) Qiao, B. T.; Wang, A. Q.; Yang, X. F.; Allard, L. F.; Jiang, Z.; Cui, Y. T.; Liu, J. Y.; Li, J.; Zhang, T. *Nat. Chem.* **2011**, *3*, 634−641.